Supporting Information

Martinez et al. 10.1073/pnas.1112849108

SI Text

1. SI Materials and Methods. ***1.1 Preparation of dMR monolayers on glass substrates.*** Thorough cleaning of glass plates is essential from the standpoint of obtaining uniform responsive dMR monolayers. For this, the glass plates are first cleaned by scrubbing the glass surface using a soft brush and detergent to wash away oils and remove large particles. The glass is then rinsed with deionized water and dried with compressed nitrogen gas. We then sonicate the substrate sequentially in acetone, isopropanol, and deionized water (five minutes each). We then dry the substrates again using compressed nitrogen gas. Plasma cleaning is then performed in a vacuum chamber with the plasma discharge at a pressure of approximately 1 mTorr, voltage of 3 kV, and a 50 mA current. The glass substrates are exposed to the plasma for about 20 min, which allows for a complete removal of the residual organic surface contaminants. To obtain the photosensitive surface monolayer on the glass plates, we submerge them into approximately a 1 wt.% solution of 2-(4-dimethylamino-phenylazo)-N-(3-triethoxysilane-propyl)-benzamide (dMR) (ref. 1) in toluene at elevated temperature of 45 °C for 90 min to facilitate surface bonding of the dMR molecules (Fig. S1). This is followed by a toluene rinse to wash away the excess dMR, blowing with dry nitrogen, and curing at 115 °C for 2 h. These dMR-decorated glass substrates are then used for preparation of cells as described in the *Methods* section of the main text.

1.2. Colloidal particles. The used melamine resin particles were obtained from Invitrogen in the form of an aqueous dispersion. Silver nanorods (nanowires) of 100 nm in diameter were obtained from Nanogap. Glass microrods of 3 μm in diameter were obtained from Duke Scientific Corp. Silica microspheres were obtained in a powder form from Fluka. Gallium Nitride (GaN) nanorods were provided by Kris Bertness from NIST (Boulder) and had about 10 μm in length and a hexagonal cross-section with approximately 150 nm edge sides (2, 3). The GaN nanorods are first dispersed in isopropanol and then transferred into the liquid crystal (LC) by mixing and letting isopropanol evaporate by heating the mixture to about 60 °C (4).

2. Laser Scanning System Integrated with Holographic Optical Tweezers. For illumination by laser beam scanning, we use an Ar laser beam at 488 nm and scanned mirrors of the confocal imaging system FV-300 from Olympus integrated with holographic optical tweezers (HOT). This integrated setup is built around an inverted IX81 optical microscope from Olympus and is schematically shown in Fig. S2. In the HOT part of the setup, the beam from an Ytterbium-doped fiber laser (1064 nm, IPG Photonics) is linearly polarized before it is expanded by a telescope [lenses L_1 (100 mm) and L_2 (250 mm)] to overfill the active area of the phase-only spatial light modulator (SLM, from Boulder Nonlinear Systems). A second telescope composed of lenses L_3 (850 mm) and L_4 (400 mm) reduces the size of the beam reflected off the SLM to slightly overfill the back aperture of the oil-immersion microscope objective. The second telescope (in the so-called 4-f arrangement) also images the phase profile encoded by the SLM to the back focal plane of the microscope objective. The holograms displayed on the SLM create trap patterns in the focal plane of the microscope objective. A dichroic mirror (from Chroma) is used to reflect the trapping laser beam into the microscope objective. By displaying holograms on the SLM, the phase of the reflected light is controlled between 0 and 2π on a pixel-by-pixel basis. The SLM has 512×512 pixels, each of size 15×15 μm^2. New holograms can be generated on the SLM at a rate of 10–30 Hz. The positions of the traps are defined by the calculated holograms and controlled by the HOT software (Arryx, Inc.). Bright-field imaging with visible light is performed using a charge-coupled device (CCD) camera (Pointgrey, Flea 2, IEEE 1394b).

3. Free Energy of Director Structures in Cells with Light-Controlled Boundary Conditions. The behavior of LC domains in response to the changes of surface boundary conditions as well as the manipulation of colloids dispersed in the nematic LC can be understood by considering the bulk elastic energy for the light-dictated surface boundary conditions controlled through the dMR surface monolayers. The Frank elastic energy of LCs can be expressed in terms of spatial gradients of the director field $\mathbf{N}(\mathbf{r})$ as follows (56)

$$U_{\mathrm{el}} = \int d^3\mathbf{r}\left[\frac{K_{11}}{2}(\nabla\cdot\mathbf{N})^2 + \frac{K_{22}}{2}(\mathbf{N}\cdot(\nabla\times\mathbf{N}))^2 + \frac{K_{33}}{2}(\mathbf{N}\times(\nabla\times\mathbf{N}))^2\right],$$

where K_{11}, K_{22}, and K_{33} are three independent Frank elastic constants corresponding to "splay," "twist," and "bend" deformations, respectively, and the integration is carried out over the volume of the LC confined in the cell. Typically, the three elastic constants of thermotropic small molecule nematic materials are of the same order of magnitude. Therefore, one often introduces the so-called one-elastic-constant approximation $K = (K_{11} + K_{22} + K_{33})/3$. For 5CB at room temperature $K_{11} \approx 6.4$ pN, $K_{22} \approx 3$ pN, $K_{33} \approx 10$ pN, and $K \approx 6.5$ pN. We use analytical estimates of elastic energies involved in the optoelastic manipulation, as discussed in the main text, as well as numerical minimization of U_{el} (without the one-constant approximation) in order to obtain the static equilibrium and metastable director configurations in confined LC cells with light-controlled boundary conditions (Fig. 5*B* and Fig. S3 *H* and *I*). This numerical minimization of U_{el} is implemented by use of Mathematica 8 software (obtained from Wolfram) with the assumption of infinitely strong surface anchoring boundary conditions.

4. Effects of Gravity. In the LC cell with a uniform far-field director, elastic forces balance the gravitational force acting on a colloidal particle such as an elastic dipole formed by a sphere with vertical boundary conditions (Fig. 2*F*). These elastic forces repel the particle from the bounding plates with strong surface boundary conditions, so that the particle tends to localize in the LC cell midplane at vertical position $z = h/2$ (h is the LC cell thickness), although gravity can displace it downward from this plane. This balance of forces can be expressed as $F_g = F_0 - F_h$, where F_g is the force due to gravity and F_0 and F_h are the elastic forces originating due to the strong planar anchoring on the substrates at $z = 0$ and $z = h$. In analogy with electrostatics, the interaction of elastic dipoles with bounding plates can be modeled using the method of images (7, 8). By using a simple approximation of having two image elastic dipoles on the opposite sides of the confining glass plates, the balance can be written explicitly in terms of the particle displacement from the cell midplane, δ (7):

$$\frac{4}{3}\pi R^3 \Delta\rho g = \frac{3}{2}\pi K C^2\left(\frac{2R}{h-2\delta}\right)^4 - \frac{3}{2}\pi K C^2\left(\frac{2R}{h+2\delta}\right)^4,$$

where C is a numerical factor, $\Delta\rho$ is the difference between the densities of the particle and the host LC fluid, and R is the particle radius. Using this expression, we have plotted the relative displacement δ/h as a function of $\Delta\rho$ and R for three different cell thicknesses h (Fig. S8). The results show that even particles having density much higher than that of typical LC materials, like those made of silver, can be localized very close to the cell midplane with δ/h being close to 1%, provided that relatively thin LC cells of $h \leq 5$ μm are used (Fig. S8). Clearly, the particles levitate in the LC bulk as gravity is balanced by the strong surface wall-dipole elastic repulsion. Interestingly, the vertical displacement due to gravity is more pronounced for smaller particles than for the ones of bigger size. This result is somewhat counterintuitive and is very different from the case of conventional optical trapping where gravitational forces preclude manipulation of bigger particles (tens of micrometers and larger). However, this finding can be explained by the fact that the elastic force scales with the particle size as R^4 but the gravitational force scales as R^3, so that elastic forces dominate in the case of larger particles and localize them closer to the cell midplane. Therefore, unlike in the case of trapping by use of optical gradient forces, gravitational forces do not set the upper limit for the size of a particle that can be manipulated using the optoelastic approach. Importantly, although δ/h can be substantial (especially in the thick cells), this relative displacement only somewhat modifies optoelastic manipulation. For example, in the case of a noticeable vertical displacement from the cell midplane, the colloidal structures in thick LC cells shown in Fig. 2 *A–E* would be rotated by an angle different from half the angle to which the easy axis at one of the confining glass plates is rotated. This, however, does not preclude or limit the optoelastic manipulation of particles in any way. Although the plots in Fig. S8 have been obtained for a range of particle sizes within (10–5,000) nm, particles of small size $R < 50$ nm (i.e., smaller than the surface anchoring extrapolation length) might not support the dipolar structure shown in Fig. 2*F* and a more rigorous analysis of the effects of gravitational forces on nanoparticles in LCs and how they can be balanced by wall-particle elastic forces would require a detailed knowledge of the director field around such colloids. Although the above analysis was focused on spherical particles with vertical surface anchoring and dipolar elastic distortions, it can be extended to particles of other shapes and with different surface boundary conditions while yielding qualitatively similar conclusions (8, 9).

5. Force Characterization. Optoelastic forces are characterized using two complementary approaches. In the first approach, we utilize a holographic laser trapping system with calibrated force vs. power dependence (Figs. S2 and S7). For the laser manipulation, we use circularly-polarized 1064 nm infrared beams to mitigate the effects of polarization dependence of optical gradient forces in LCs (10). We control $\mathbf{N}(\mathbf{r})$ by inducing various elastic distortions through the structured illumination of dMR (Fig. 1 *B–F*) and then probe the landscape of ensuing optoelastic forces by slowly moving trapped particles by laser tweezers. From the balance of laser trapping forces and optically controlled elastic forces, we determine the latter.

In the second approach, the optoelastic forces are characterized directly by use of their balance with viscous forces when video tracking particle motion due to elastic interactions. Starting from a uniformly aligned sample, we illuminate an area near a colloidal particle using the projection system and thus locally distort $\mathbf{N}(\mathbf{r})$. Depending on the symmetry of optically-induced distortions and those around the inclusion, the interaction between a particle and a barrier is either attractive, in which case the colloid moves toward the region with distorted $\mathbf{N}(\mathbf{r})$ until it comes to rest within it (Fig. 5*A*), or repulsive—thus pushing the colloid away from the distortion until the elastic interactions become comparable to thermal fluctuations. We track the particle positions vs. time (Fig. 5*C*, *Inset*) and determine their velocity v. We neglect the inertia effects (since particle motion is overdamped) and determine the optoelastic force from its balance with the Stokes' viscous drag force $F_{oe} = 6\pi\eta_{eff}Rv$ (Fig. 5*C*), where η_{eff} is the effective viscosity coefficient for the particle with the surrounding "corona" of $\mathbf{N}(\mathbf{r})$-distortions. η_{eff} depends on the motion direction of the particle with respect to $\mathbf{N}_0$ and on whether $\mathbf{N}(\mathbf{r})$ is relatively uniform or has dipolar or quadrupolar structure. For example, $\eta_{eff} = 86.4$ mPa · s for a particle with dipolar $\mathbf{N}(\mathbf{r})$ in 5CB (Fig. 2*F*) when measured for the particle motion orthogonal to $\mathbf{N}_0$ (5). Typical dependencies of F_{oe} and trap stiffness on the amount of $\mathbf{N}(\mathbf{r})$-twist across the cell in the trap are shown in Fig. 5.

1. Yi Y, Farrow MJ, Korblova E, Walba DM, Furtak TE (2009) High-sensitivity aminoazobenzene chemisorbed monolayers for photoalignment of liquid crystals. *Langmuir* 25:997–1003.
2. Bertness KA, et al. (2008) Mechanism for spontaneous growth of GaN nanowires with molecular beam epitaxy. *J Cryst Growth* 310:3154–3158.
3. Schlager JB, et al. Steady-state and time-resolved photoluminescence from relaxed and strained GaN nanowires grown by catalyst-free molecular-beam epitaxy. *J Appl Phys* 103:124309.
4. Trivedi RP, Lee T, Bertness K, Smalyukh II (2010) Three dimensional optical manipulation and structural imaging of soft materials by use of laser tweezers and multimodal nonlinear microscopy. *Opt Express* 18:27658–27669.
5. Stark H, Ventzki D (2001) Stokes drag of spherical particles in a nematic environment at low Ericksen numbers. *Phys Rev E* 64:031711.
6. de Gennes PG, Prost J (1995)*The Physics of Liquid Crystals*, New York, Oxford University Press.
7. Pishnyak OP, Tang S, Kelly JR, Shiyanovskii SV, Lavrentovich OD (2007) Levitation, lift, and bidirectional motion of colloidal particles in an electrically driven nematic liquid crystal. *Phys Rev Lett* 99:127802.
8. Pergamenshchik VMV, Uzunova VA (2009) Colloid-wall interaction in a nematic liquid crystal: The mirror-image method of colloidal nematostatics. *Phys Rev E* 79:021704.
9. Lapointe C, et al. (2004) Elastic torque and the levitation of metal wires by a nematic liquid crystal. *Science* 303:652–655.
10. Trivedi RP, Engström D, Smalyukh II (2011) Optical manipulation of colloids and defect structures in anisotropic liquid crystal fluids. *J Opt* 13:044001.

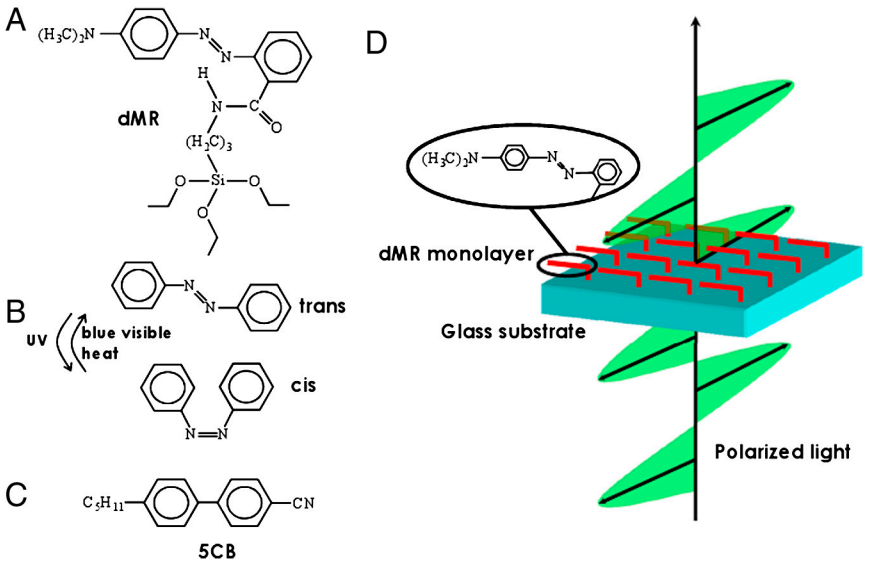

Fig. S1. Chemical structures of used molecules and schematics of optical control of the dMR surface monolayers. (*A*) Molecular structure of the dMR. (*B*) Azobenzene moiety of the dMR in the *trans*- and *cis*- states. (*C*) Molecular structure of pentylcyanobiphenyl (5CB). (*D*) A schematic depicting the photo-alignment of dMR molecules within a surface monolayer using polarized incident light.

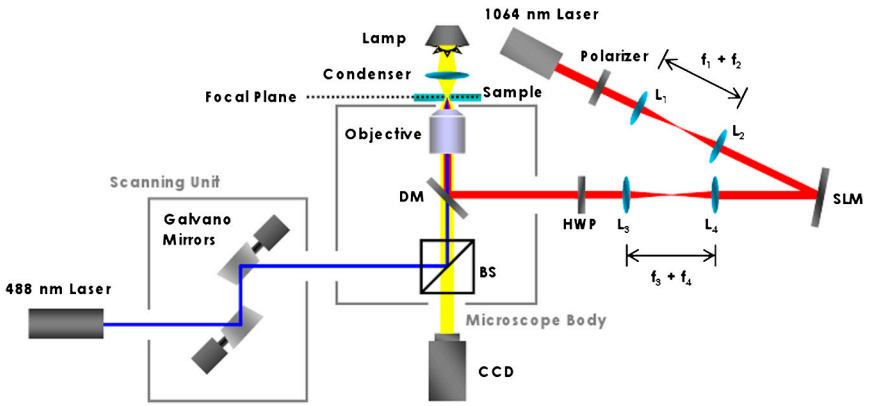

Fig. S2. Schematic of the integrated laser-scanning illumination and holographic optical trapping system. Integrated setup of the conventional optical trapping and the laser-scanning illumination system is built around an inverted Olympus IX81 microscope. The laser trapping system utilizes a 1064 nm laser and a spatial light modulator (SLM). The laser scanning system is a part of the FV-300 Olympus Fluoview confocal scanning unit and controls the lateral patterns of a scanned focused 488 nm Ar ion laser beam used for patterned structuring of $\mathbf{N}(\mathbf{r})$ through the control of dMR monolayers.

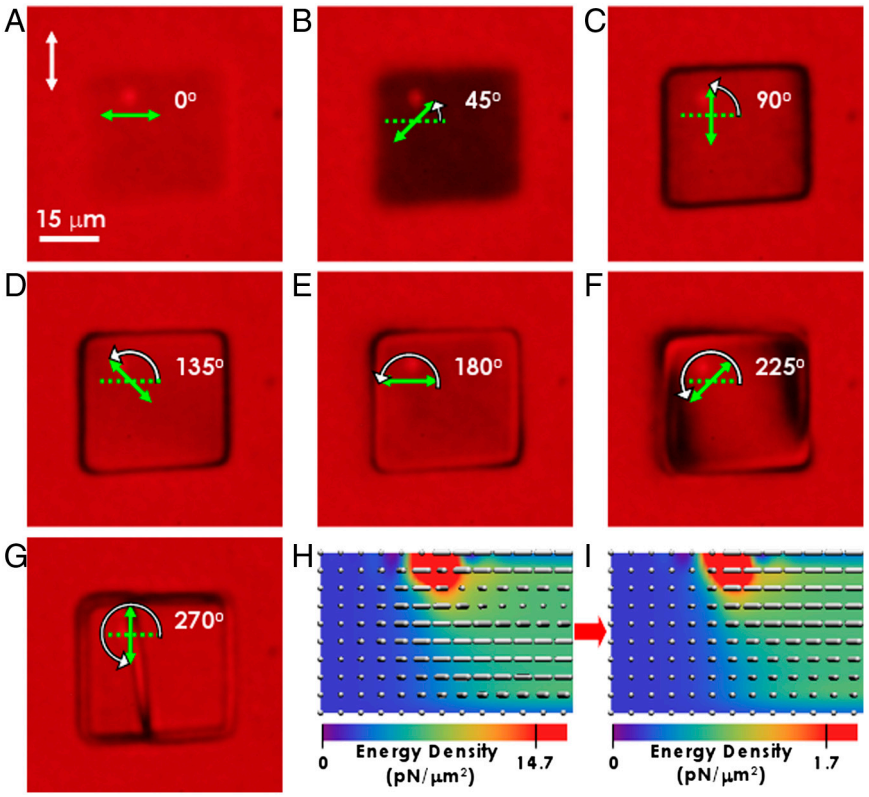

Fig. S3. Relaxation of elastic distortions in strongly twisted nematic domains. (*A*–*G*) A square region within a uniformly twisted sample is illuminated with blue light having linear polarization direction indicated by the green double arrows. Continuous rotation of the light polarization as marked on the images changes the amount of twist inside the illuminated square. As the bulk elastic energy increases with increasing the amount of twist, (*G*) a line defect within the LC domains propagates to minimize energy via transformation of the structure into the one with a less twisted state. (*H*, *I*) director structures (depicted by use of cylinders) and elastic energy densities (shown using the color scales) for (*H*) a domain with the light-induced $3\pi/2$-twist distortion and (*I*) a relaxed state with the $\pi/2$-twist obtained after propagation of the defect line that relieves some of the distortions by transforming it to the less twisted state. The polarizing microscopy images (*A*–*G*) have been obtained between uncrossed polarizers and using red probing light. The vertical cross-sections of the sample shown in (*H*, *I*) are obtained by numerical minimization of elastic free energy and correspond to the experimental image shown in (*G*) for cases before and after the defect line propagation.

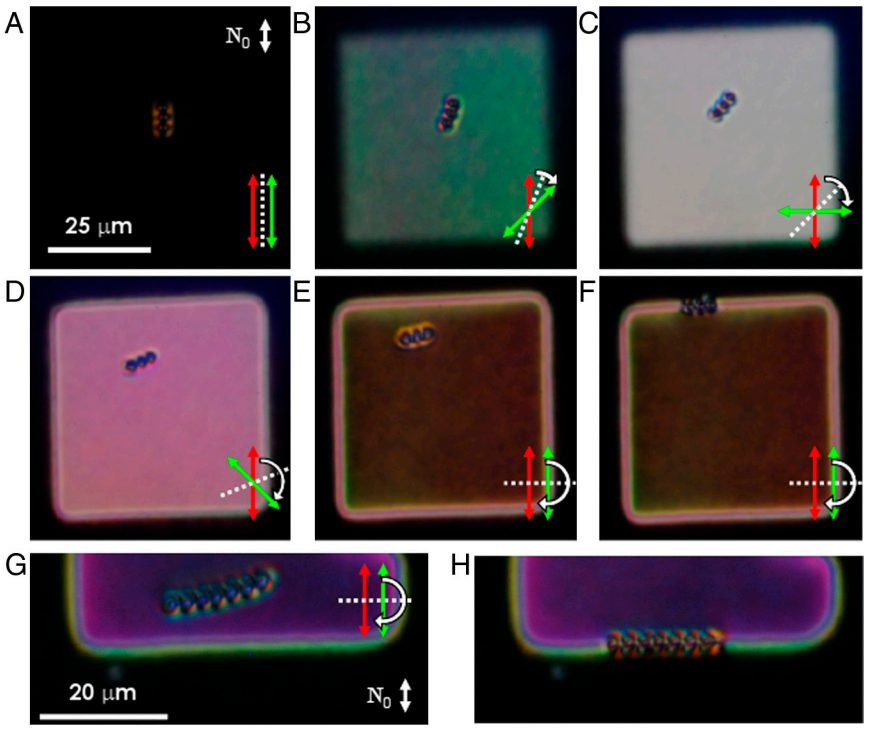

Fig. S4. Optoelastic control of colloidal self-assemblies. (*A*) A dipolar chain in a uniform sample oriented along $\mathbf{N}_0$ (white double arrow). The red arrow represents the orientation of the trans-state azobenzene of dMR molecules and director at the bottom substrate within the square domain, while the green arrow represents their orientations at the top substrate. The director orientation in the central plane is shown by the white dotted line. (*B–F*) As the polarization of the projected illumination is rotated clockwise, the trans-state dMR molecules and **N** at the top substrate follow but remain unchanged at the bottom surface. The orientation of **N** and that of a colloidal chain in the middle plane is halfway between the bottom and top surfaces. Note that rotation of the chain in (*B–F*) is taking place simultaneously with its attraction to the boundary between twisted and untwisted domains, similar to that shown in Fig. 5*A* for an individual particle. (*G*, *H*) Images showing attraction of a long colloidal chain to the boundary between π-twisted and untwisted LC domains.

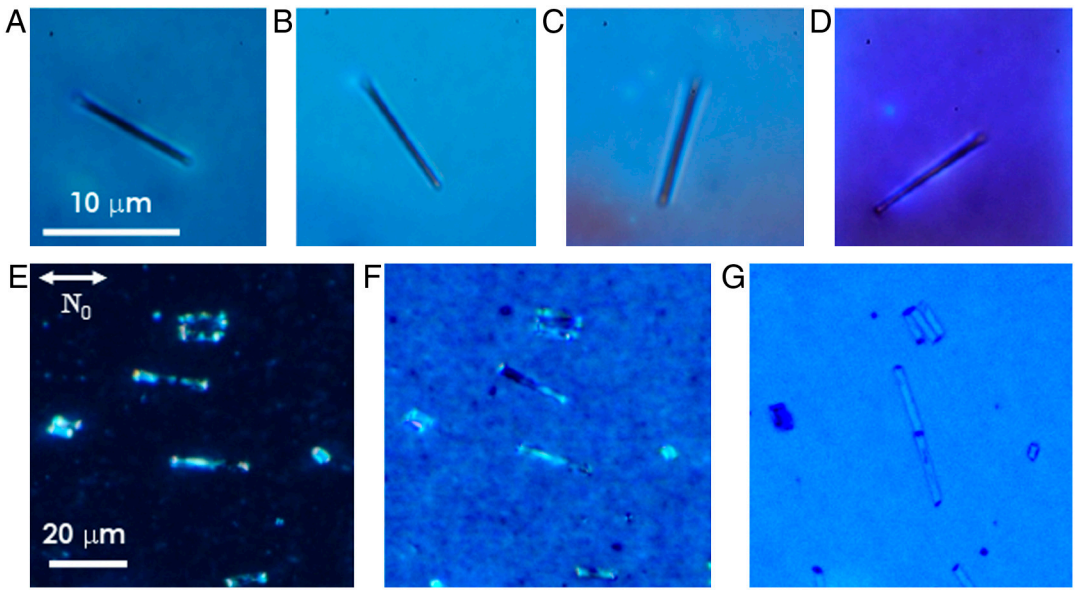

Fig. S5. Optoelastic rotation of rods of various material compositions. (*A–D*) Gallium nitride nanowire rotating with the local **N** as polarization of the illumination light and azobenzene molecules within the surface monolayer are rotated. (*E–G*) Simultaneous rotation of glass rods using the laser scanning system. The used illumination source is an Ar ion laser (488 nm) from the laser scanning system shown in Fig. S2.

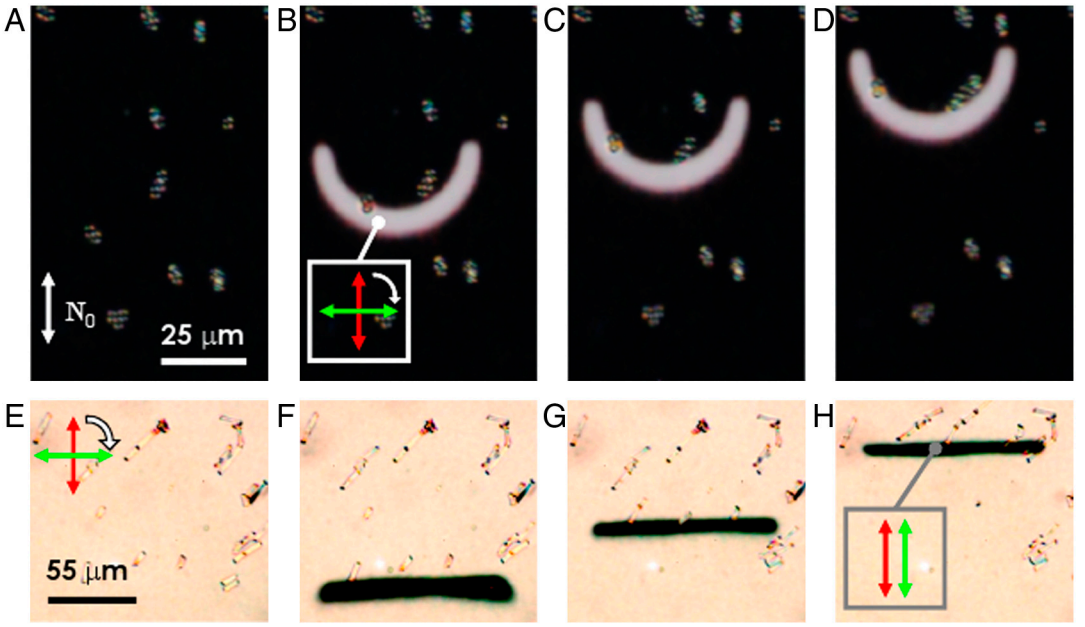

Fig. S6. Translation of various colloids by use of optically controlled twisted and untwisted domains. (*A*) Melamine resin spheres (3 μm in diameter) dispersed within the LC with a uniform alignment along $\mathbf{N}_0$. (*B–D*) Translation of the spheres by use of a semicircle pattern focused onto a dMR-decorated cell substrate. The polarization of the projected light is rotated to create a 90° twisted director structure within the semicircle domain as depicted by the red and green arrows showing **N** at the bottom and top substrates, respectively. The semicircle-shaped trap effectively collects and moves the particles as the projected pattern is translated laterally. (*E*) A dispersion of 3 μm diameter glass rods in a cell with a 90°-twisted director. (*F–H*) Translation of an untwisted rectangular LC domain (obtained by adjusting the polarization of the corresponding projected illumination pattern) allows for an effective translation of the rods trapped at the domain interface.

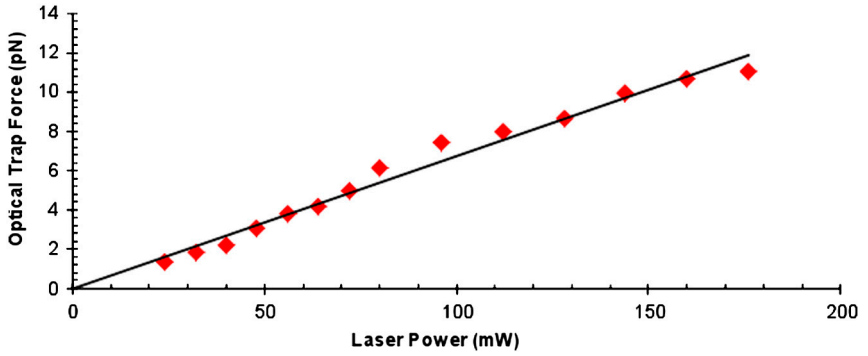

Fig. S7. Calibrated trap escape force vs. laser power of a circularly-polarized 1064 nm laser beam used to probe optoelastic forces. The dependence is obtained for melamine resin spheres (3 μm in diameter) dragged through the 5CB at increasingly higher velocities: as the particle barely escapes from the trap, the optical trap escape force is equal to the calculated Stokes drag force.

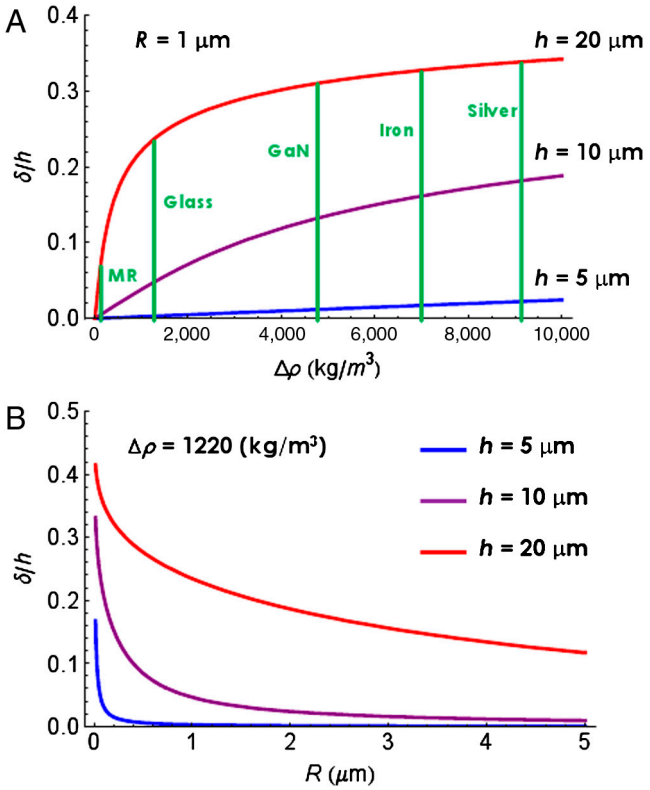

Fig. S8. Displacement of nanoparticles from the LC cell midplane due to gravity. (*A*) Relative displacement vs. mismatch of density of a colloidal particle and the LC host for different cell thicknesses *h*; the vertical green lines mark the values of density mismatch $\Delta\rho$ between density of different particle materials and that of 5CB. In the images in Fig. S8 "MR" stands for melamine resin and "GaN" stands for Gallium Nitride. (*B*) Relative displacement as a function of particle radius *R* for different *h* for the case of silica spheres in 5CB.